Microscopic exploration of electronic states in an insulator phase of the novel nodal-line semimetal [Ni(hfdt)$_2$]

Takahiko Sekine[1], Taiki Kawamura[2]
[1] *Department of Applied Physics, University of Tokyo*,
[2] *Department of Physics, Nagoya University*

2022 年 12 月 13 日

Authors

Takahiko Sekine: his research field is a resistivity measurement and an nuclear magnetic resonance measurement on the Dirac electron systems.

Taiki Kawamura: his research field is a theoretical calculation of an electron correlation effect in the Dirac electron system.

1 Abstract

Electrons with cone-shape energy-momentum dispersions behave as massless particles in solids. The vertexes of the cone-shape dispersions are dubbed the Dirac points and the Dirac points continuously connected in lines in the three-dimensional (3D) Brillouin zone are Dirac nodal lines (NLs). A single-component molecular conductor [Ni(hfdt)$_2$], which demonstrated a crossover from a low-pressure insulating phase to a high-pressure metallic phase at 8 GPa pressure [1], was theoretically suggested to host Dirac NLs in the high-pressure phase. However, the details of the Dirac NLs, let alone the electronic state in the low-pressure phase, have not understood yet. The purpose of the present study is to elucidate the electronic state of [Ni(hfdt)$_2$] at ambient pressure. Kawamura in Nagoya University theoretically analyzed the electronic state with the extended Hubbard model. Sekine in Unversity of Tokyo performed a ^{19}F nuclear magnetic resonance (NMR) experiment.

Kawamura *et al.* applied a mean-field approximation to the extended Hubbard model for [Ni(hfdt)$_2$] and calculated its ground state. From the calculation without Coulomb interactions, they showed a crossover from a metallic state to an insulator state at lower pressure than reported in the previous study [1]. The existence of two Dirac NLs is also verified in the high-pressure metallic phase. The present analysis reproduced the

crossover pressure reported in the previous study by introducing an on-site Coulomb interaction U and an intersite Coulomb interaction V and discovered that [Ni(hfdt)$_2$] is a band insulator with a finite band gap at the ambient pressure. Furthermore, the theoretical results suggested the probability of an intramolecular antiferromagnetic state if the value of V is taken smaller than that reproducing the crossover pressure.

To verify the theoretical indication, we performed the ^{19}F-NMR experiment using a polycrystalline sample of [Ni(hfdt)$_2$]. The obtained spectra did not indicate any symptoms of a magnetic ordered state under every magnetic field of 0.75, 2.5 and 7.5 T. Temperature dependence of the nuclear spin-lattice relaxation rate $1/T_1$ was reproduced well by Bloembergen-Purcell-Pound (BPP) model, which revealed that a rotational motion of CF_3 groups dominated $1/T_1$ above 80 K. Enhancement of spin fluctuations as indication of a magnetic transition was not observed. [Ni(hfdt)$_2$] can be considered as a non-magnetic insulator at ambient pressure, consistent with the band insulator state calculated by the extended Hubbard model using the values of U and V reproducing the crossover pressure in the previous study.

2 Background and purpose

Dirac electrons described as pseudorelativistic massless quasiparticls in solids are of great interest due to the quite different properties from ordinary metals and semiconductors such as an ultrahigh mobility and an anomalous Landau quantization. The Dirac electron systems host the band structures with cone-shape energy-momentum dispersions (Dirac cones), which have been observed in a monolayer Graphite (Graphene) and in a layered molecular conductor α-(BEDT-TTF)$_2$I$_3$. Among the Dirac electron materials, the molecular materials are good for detailed explorations of the properties of the Dirac electrons in the vicinity of the Fermi energy since they usually include less impurities and defects. Recently, the Dirac electrons in the single-component molecular materials have attracted much attentions. Band calculations exhibited that the single-component molecular conductors [Pd(dddt)$_2$] under pressure [2] and [M(dmdt)$_2$] (M = Ni or Pt)[3] host the Dirac cone-type band structures in the vicinity of the Fermi energy. These systems are different from the Dirac electron systems such as Grephene and α-(BEDT-TTF)$_2$I$_3$ in terms of the vertexes of the Dirac cone-type band structures (Dirac points) continuously connected in lines in the first Brillouin zone. This is the Dirac nodal line (NL) and the materials with the Dirac NLs are called NL semimetals. In the NL semimetals, novel electronic states are expected to emerge such as Landau-quantized subbands and drumhead-type surface states, advanced from the conventional the Dirac electrons.

Akito Kobayashi *et al.* in Nagoya University theoretically predicted that [Ni(hfdt)$_2$] (hfdt = bis (trifluoromethyl) tetrathiafulvalenedithiolate), which is an insulator at ambient pressure, is a new NL semimetal under high pressure. The remarkable character of this material is to show a superconducting transition at 8 GPa pressure. There is no other example of the Dirac NL system with a superconducting phase. [Ni(hfdt)$_2$] is expected to be a platform to study novel physical properties of the Dirac NLs. While the electronic state under pressure is highly anticipated, the electronic state at an ambient pressure is still unclear. The resistivity measurement reported an insulating behavior [1]. [Ni(hfdt)$_2$] has been considered as a band insulator with about 0.2 eV band gap so far, but the details of the electronic state have not been verified yet.

Here, in order to understand the nature of the physical property, it is an urgent task to elucidate the electronic state in the ambient insulator phase. In the present study, we aim to reveal the ambient electronic state of [Ni(hfdt)$_2$] by combining the theoretical calculation involving the electron correlation effects with the experiment using the microscopic probe. First, we introduce the analysis of the electronic state with the extended Hubbard model by Kawamura in Nagoya University. Second, we describe the results of ^{19}F-NMR experiment by Sekine in University of Tokyo.

3 Analyses of electronic states by the extended Hubbard model

3.1 Method

The analyses of the band structure by the first-principles calculations and of the electronic state of [Ni(hfdt)$_2$] using the extended Hubbard model were conducted by Kawamura and Masaki Saito in Kobayashi laboratory of Nagoya University. Using the data of the crystal structure of [Ni(hfdt$_2$)] measured by the X-ray diffraction experiment, the first-principles calculations were conducted with the open source code Quantum ESPRESSO to obtain the energy-momentum dispersions. Wannier fitting to the three band in the vicinity of the Fermi energy was performed to determine the Wannier functions and the values of the transfer integrals. A free software RESPACK was used for the Wannier fitting and estimation of the Coulomb interactions. A tight-binding-model Hamiltonian was constructed using the Wannier functions and the transfer integrals, and then the extended Hubbard-model Hamiltonian was constructed by introducing the on-site Coulomb interaction U and the intersite Coulomb interaction V to the tight-binding-model Hamiltonian. With parameterizing the values of U and V, the electronic state under pressure was examined.

The Hamiltonian of the extended Hubbard model is as follows;

$$\begin{aligned} \mathcal{H} &= \mathcal{H}_0 + \mathcal{H}_{\text{int}} && (1) \\ \mathcal{H}_0 &= \sum_{i,j} \sum_{\alpha,\beta} \sum_{\sigma} t_{i,\alpha;j,\beta} a^{\dagger}_{i,\alpha,\sigma} a_{j,\beta,\sigma} && (2) \\ \mathcal{H}_{\text{int}} &= \sum_{i} \sum_{\alpha} U_{\alpha} a^{\dagger}_{i,\alpha,\uparrow} a^{\dagger}_{i,\alpha,\downarrow} a_{i,\alpha,\downarrow} a_{i,\alpha,\uparrow} \\ &\quad + \frac{1}{2} \sum_{i,j} \sum_{\alpha,\beta} \sum_{\sigma,\sigma'} V_{i,\alpha;j,\beta} a^{\dagger}_{i,\alpha,\sigma} a^{\dagger}_{j,\beta,\sigma'} a_{j,\beta,\sigma'} a_{i,\alpha,\sigma} && (3) \end{aligned}$$

The first term of equation (1) is the tight-binding-model Hamiltonian and the second term is the Coulomb interaction term. $i(j)$, $\alpha(\beta)$, and $\sigma(\sigma')$ refer to the unit cell, the Wannier function and electron spin, respectively. $t_{i,\alpha;j,\beta}$ is the transfer integral from the Wannier function α in the i-th unit cell to the Wannier function β in the j-th unit cell. Using the Fourier series expansion of the creation and annihilation operators $\left(a^{(\dagger)i,\alpha,\sigma} = \frac{1}{\sqrt{N}}\sum_{\boldsymbol{k}} e^{(-)i\boldsymbol{k}\cdot\boldsymbol{r}_i} a^{(\dagger)}_{\boldsymbol{k},\alpha,\sigma}\right)$, equation (2) is diagonalized for a wavenumber $\boldsymbol{k}$ as

$$\mathcal{H}_0 = \sum_{\boldsymbol{k}} \sum_{\alpha,\beta,\sigma} \varepsilon(\boldsymbol{k}) a^\dagger_{\boldsymbol{k},\alpha,\sigma} a_{\boldsymbol{k},\beta,\sigma} \tag{4}$$

$$\left(\varepsilon(\boldsymbol{k}) = \sum_{i,j} t_{i,\alpha;j,\beta} e^{-i\boldsymbol{k}\cdot(\boldsymbol{r}_i-\boldsymbol{r}_j)}\right) \tag{5}$$

The Wannier fitting optimizes the Wannier functions and $t_{i,\alpha;j,\beta}$ to make the dispersion of the eigenenergy of this Hamiltonian correspond with the energy-momentum dispersion from the first-principles calculations.

A mean-field approximations are applied to the Fourier series expansions of equation (3). The first term of equation (3) is expanded as

$$\begin{aligned}
&\frac{1}{N^2}\sum_i \sum_{\boldsymbol{k_1},\boldsymbol{k_2},\boldsymbol{k_3},\boldsymbol{k_4}} a^\dagger_{\boldsymbol{k}_1,\alpha,\uparrow} a^\dagger_{\boldsymbol{k}_2,\alpha,\downarrow} a_{\boldsymbol{k}_4,\alpha,\downarrow} a_{\boldsymbol{k}_3,\alpha,\uparrow} e^{i(\boldsymbol{k_3}+\boldsymbol{k_4}-\boldsymbol{k_1}-\boldsymbol{k_2})\cdot\boldsymbol{r}_i} \\
= \; &\frac{1}{N}\sum_{\boldsymbol{k},\boldsymbol{k'},\boldsymbol{q}} a^\dagger_{\boldsymbol{k}-\boldsymbol{q},\alpha,\uparrow} a^\dagger_{\boldsymbol{k'}+\boldsymbol{q},\alpha,\downarrow} a_{\boldsymbol{k'},\alpha,\downarrow} a_{\boldsymbol{k},\alpha,\uparrow} \\
\approx \; &\frac{1}{N}\sum_{\boldsymbol{k},\boldsymbol{k'},\boldsymbol{q}} a^\dagger_{\boldsymbol{k}-\boldsymbol{q},\alpha,\uparrow} a_{\boldsymbol{k},\alpha,\uparrow} \left\langle a_{\boldsymbol{k'}+\boldsymbol{q},\alpha,\downarrow} a_{\boldsymbol{k'},\alpha,\downarrow}\right\rangle + \left\langle a^\dagger_{\boldsymbol{k}-\boldsymbol{q},\alpha,\uparrow} a_{\boldsymbol{k},\alpha,\uparrow}\right\rangle a_{\boldsymbol{k'}+\boldsymbol{q},\alpha,\downarrow} a_{\boldsymbol{k'},\alpha,\downarrow} \\
&\qquad - \left\langle a^\dagger_{\boldsymbol{k}-\boldsymbol{q},\alpha,\uparrow} a_{\boldsymbol{k},\alpha,\uparrow}\right\rangle \left\langle a_{\boldsymbol{k'}+\boldsymbol{q},\alpha,\downarrow} a_{\boldsymbol{k'},\alpha,\downarrow}\right\rangle \\
= \; &\frac{1}{N}\sum_{\boldsymbol{k},\boldsymbol{k'}} a^\dagger_{\boldsymbol{k},\alpha,\uparrow} a_{\boldsymbol{k},\alpha,\uparrow} \left\langle a_{\boldsymbol{k'},\alpha,\downarrow} a_{\boldsymbol{k'},\alpha,\downarrow}\right\rangle + \left\langle a^\dagger_{\boldsymbol{k},\alpha,\uparrow} a_{\boldsymbol{k},\alpha,\uparrow}\right\rangle a_{\boldsymbol{k'},\alpha,\downarrow} a_{\boldsymbol{k'},\alpha,\downarrow} \\
&\qquad - \left\langle a^\dagger_{\boldsymbol{k},\alpha,\uparrow} a_{\boldsymbol{k},\alpha,\uparrow}\right\rangle \left\langle a_{\boldsymbol{k'},\alpha,\downarrow} a_{\boldsymbol{k'},\alpha,\downarrow}\right\rangle
\end{aligned} \tag{6}$$

where $\boldsymbol{k_1} - \boldsymbol{k_3} = \boldsymbol{k_4} - \boldsymbol{k_2} = \boldsymbol{q}$. In the last transformation, the orthogonality of the wavenumbers is used $\left(\sum_{\boldsymbol{k},\boldsymbol{k'}} \left\langle a_{\boldsymbol{k},\alpha,\sigma} a_{\boldsymbol{k'},\alpha,\sigma}\right\rangle = \delta_{\boldsymbol{k},\boldsymbol{k'}}\right)$. The second term is also expanded as

$$\begin{aligned}
&\frac{1}{2N^2}\sum_{i,j}\sum_{\alpha,\beta}\sum_{\boldsymbol{k_1},\boldsymbol{k_2},\boldsymbol{k_3},\boldsymbol{k_4}} a^\dagger_{\boldsymbol{k}_1,\alpha,\sigma} a^\dagger_{\boldsymbol{k}_2,\beta,\sigma'} a_{\boldsymbol{k}_4,\beta,\sigma'} a_{\boldsymbol{k}_3,\alpha,\sigma} e^{i(\boldsymbol{k_3}+\boldsymbol{k_4}-\boldsymbol{k_1}-\boldsymbol{k_2})\cdot\boldsymbol{r}_i} \\
\approx \; &\frac{1}{2N^2}\sum_{i,j}\sum_{\alpha,\beta}\sum_{\boldsymbol{k},\boldsymbol{k'}} \Big\{ a^\dagger_{\boldsymbol{k},\alpha,\sigma} a_{\boldsymbol{k},\alpha,\sigma} \left\langle a_{\boldsymbol{k'},\beta,\sigma'} a_{\boldsymbol{k'},\beta,\sigma'}\right\rangle + \left\langle a^\dagger_{\boldsymbol{k},\alpha,\sigma} a_{\boldsymbol{k},\alpha,\sigma}\right\rangle a_{\boldsymbol{k'},\beta,\sigma'} a_{\boldsymbol{k'},\beta,\sigma'} \\
&\qquad - \left\langle a^\dagger_{\boldsymbol{k},\alpha,\sigma} a_{\boldsymbol{k},\alpha,\sigma}\right\rangle \left\langle a_{\boldsymbol{k'},\beta,\sigma'} a_{\boldsymbol{k'},\beta,\sigma'}\right\rangle \\
&\qquad \sum_{\boldsymbol{q}\neq 0} \Big(a^\dagger_{\boldsymbol{k}-\boldsymbol{q},\alpha,\sigma} a_{\boldsymbol{k'},\alpha,\sigma} \left\langle a_{\boldsymbol{k'}+\boldsymbol{q},\beta,\sigma'} a_{\boldsymbol{k},\beta,\sigma'}\right\rangle + \left\langle a^\dagger_{\boldsymbol{k}-\boldsymbol{q},\alpha,\sigma} a_{\boldsymbol{k'},\alpha,\sigma}\right\rangle a_{\boldsymbol{k'}+\boldsymbol{q},\beta,\sigma'} a_{\boldsymbol{k},\beta,\sigma'} \\
&\qquad - \left\langle a^\dagger_{\boldsymbol{k}-\boldsymbol{q},\alpha,\sigma} a_{\boldsymbol{k'},\alpha,\sigma}\right\rangle \left\langle a_{\boldsymbol{k'}+\boldsymbol{q},\beta,\sigma'} a_{\boldsymbol{k},\beta,\sigma'}\right\rangle e^{\boldsymbol{q}\cdot(\boldsymbol{r_i}-\boldsymbol{r_j})} \Big) \Big\} .
\end{aligned} \tag{7}$$

For simplicity, $V_{i,\alpha;j,\beta}$ is taken independent of the sites. Here, the Hartree approximation is applied, in which only the zero-$\boldsymbol{q}$ terms are used in the calculations, leading

$$\begin{aligned}\mathcal{H}_{\rm int} \approx\ & \frac{1}{N}\sum_{\boldsymbol{k}}\sum_{\alpha} U_\alpha \left[a^\dagger_{\boldsymbol{k},\alpha,\uparrow}a_{\boldsymbol{k},\alpha,\uparrow}\left\langle N_{\alpha,\downarrow}\right\rangle + \left\langle N_{\alpha,\uparrow}\right\rangle a^\dagger_{\boldsymbol{k},\alpha,\downarrow}a_{\boldsymbol{k},\alpha,\downarrow}\right] \\ & +\frac{1}{2N}\sum_{\boldsymbol{k}}\sum_{i,j}\sum_{\alpha,\beta}\sum_{\sigma,\sigma'} V_{i,\alpha;j,\beta}\left[a^\dagger_{\boldsymbol{k},\alpha,\sigma}a_{\boldsymbol{k},\alpha,\sigma}\left\langle N_{\beta,\sigma'}\right\rangle + \left\langle N_{\alpha,\sigma'}\right\rangle a^\dagger_{\boldsymbol{k},\beta,\sigma}a_{\boldsymbol{k},\beta,\sigma}\right] \\ & -\frac{1}{N}\sum_{\alpha} U_\alpha \left\langle N_{\alpha,\uparrow}\right\rangle\left\langle N_{\alpha,\downarrow}\right\rangle - \frac{1}{2N}\sum_{i,j}\sum_{\alpha,\beta}\sum_{\sigma,\sigma'}\left\langle N_{\alpha,\sigma}\right\rangle\left\langle N_{\beta,\sigma'}\right\rangle . \end{aligned} \tag{8}$$

$\left\langle N_{\alpha,\sigma}\right\rangle \left(\equiv \sum_{\boldsymbol{k}}\left\langle a^\dagger_{\boldsymbol{k},\alpha,\sigma}a_{\boldsymbol{k},\alpha,\sigma}\right\rangle\right)$ is an averaged number of electrons of spin σ on the Wannier function α. The electron filling is set to 2/3.

The crystal structure data used for the first-principles calculations are obtained by the X-ray structural analyses at ambient, 1.6 GPa, 3.8 GPa and 6.7 GPa pressures. The pressure dependence of the transfer integral was calculated by a linear interpolation of those from the Wannier fitting at each pressure.

3.2 Results and discussions

Figure 1 shows the molecular structure of Ni(hfdt)$_2$ and the crystal structure of [Ni(hfdt)$_2$]. There is only one molecule in a unit cell. Figure 1 is drawn using the data of the X-ray diffraction analysis at ambient pressure and 200 K temperature.

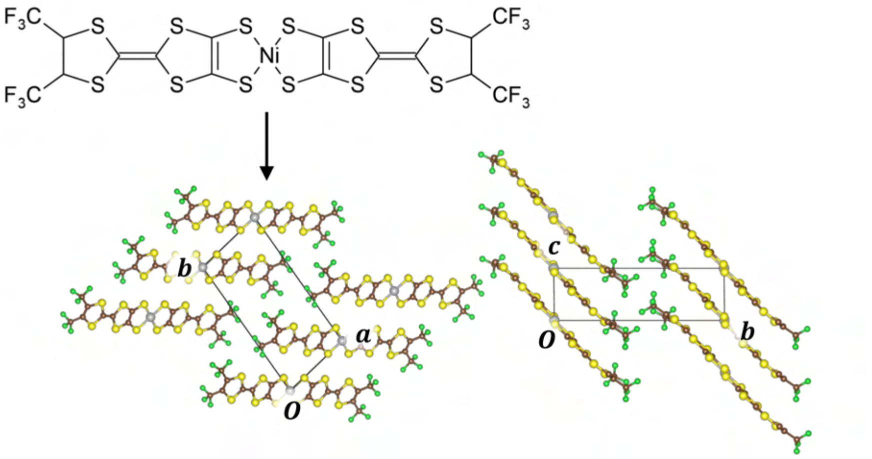

FIG. 1: Molecular structure of Ni(hfdt)$_2$ and crystal structure of [Ni(hfdt)$_2$]. There is an inversion center on Ni atom.

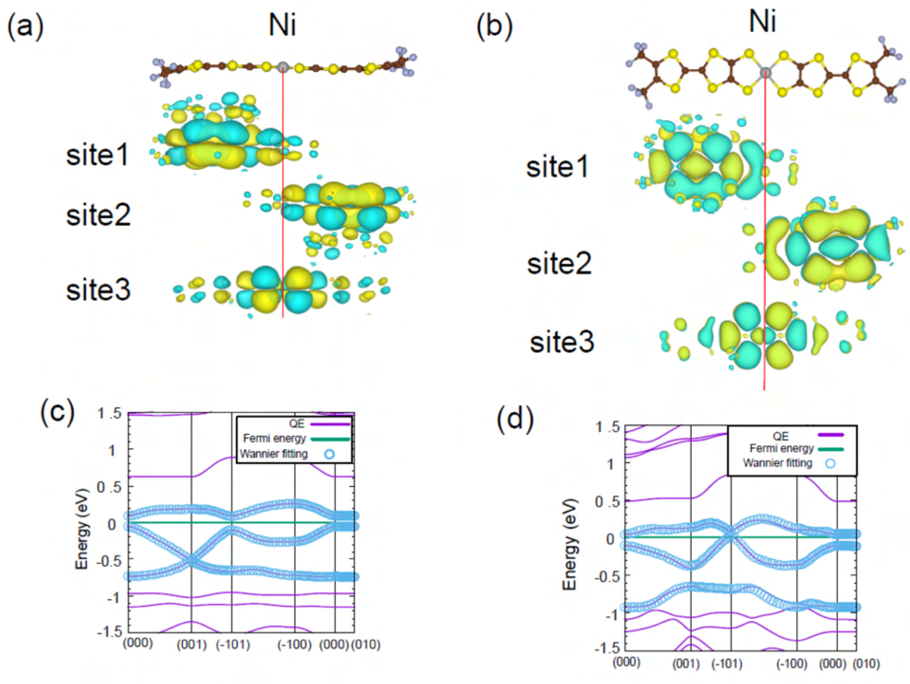

FIG. 2: Wannier orbitals of [Ni(hfdt)$_2$] obtained by the Wannier fitting(a,b). The energy-momentum dispersions from the first-principles calculations and the results of Wannier fittings at 200 K and 1bar(c) and at 293 K and 6.7 GPa(d).

Figure 2 shows the Wannier orbitals of [Ni(hfdt)$_2$] (a,b), the energy-momentum dispersions from the first-principles calculations and the results of the Wannier fitting at ambient pressure and 200 K (c), and those at at 6.7 GPa and 293 K (d). There are 3 Wannier orbitals in a unit cell. Site1 and site2 are centered on the left and right hfdt ligand, respectively, and site3 is centered on Ni atom. Site1 and site2 are exchanged with each other by an inversion operation. The first-principles calculations demonstrate that [Ni(hfdt)$_2$] is a band insulator with a finite band gap around the Fermi energy at ambient pressure and that the band gap closes at 6.7 GPa pressure indicating a transition to a metallic state. The transfer integrals used in the Wannier fitting at 6.7 GPa are shown in figure 3.

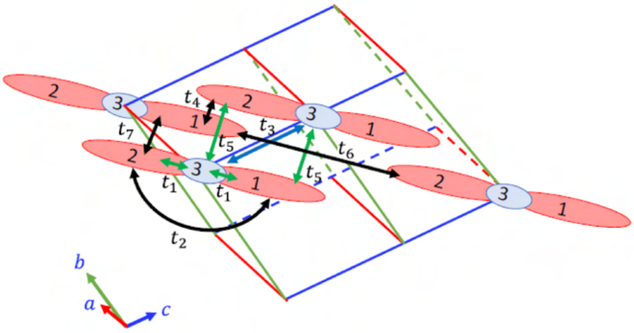

t_1	0.26662
t_2	-0.02677
t_3	-0.16973
t_4	-0.16298
t_5	0.08004
t_6	0.00862
t_7	0.03724

FIG. 3: Values of transfer integrals among site1, site2 and site3 (eV)

[Ni(hfdt)$_2$] is a strongly two-dimensional (2D) material so that the transfer integrals in the ac plane are larger than those along the b axis. The Wannier fitting involves the transfer integrals larger than 0.03 times the maximum in ac plane and t_6 that is only the transfer integral along b axis.

Figure 4 depicts the energy-momentum dispersions in 2D wavenumber space obtained by equation (2) using the Wannier functions and the transfer integrals discussed above, where the Coulomb interactions are not considered ($U = V = 0$). The energy gap is open in the entire k_a–k_c wavenumber plane at ambient pressure (a). At 6.7 GPa pressure, there are two Dirac cones, whose Dirac points are designated by the red circles (b). These two Dirac points in the k_a–k_c plane form two Dirac NLs along k_b, respectively (c). We observed merging of the two Dirac NL into a ring-shaped Dirac NL as the pressure is reduced, called Dirac nodal rings, which is spared here.

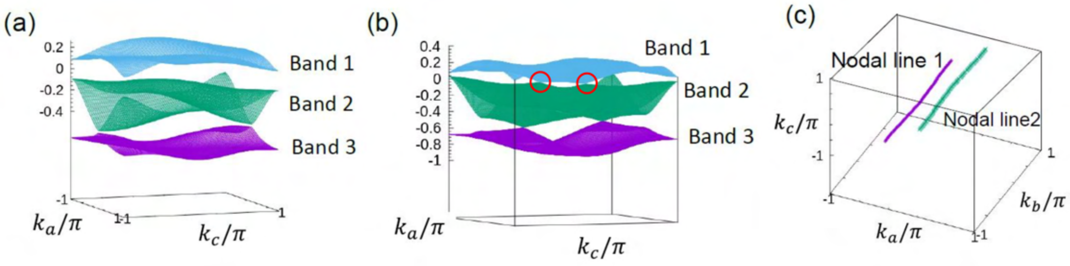

FIG. 4: Energy-momentum dispersions in the k_a–k_c wavenumber plane obtained by the calculations with the tight-binding models at ambient pressure (a) and at 6.7 GPa (b). Red circles designate the Dirac points in the vicinity of the Fermi enrergy. (c)Dirac NLs in the first Brillouin zone.

The crossover from a metallic state to an insulator state was observed at about 8 GPa pressure in the previous resistivity measurement [1], which is inconsistent with the calculation with the tight-binding model obtaining the energy gap already closed at 6.7 GPa.

On-site Coulomb interaction U is estimated approximately 1.4 eV by using RESPACK. Because the band dispersion width is approximately 1.2 eV in figure 4(b), the Coulomb interactions should play an important role in the electronic state of [Ni(hfdt)$_2$].

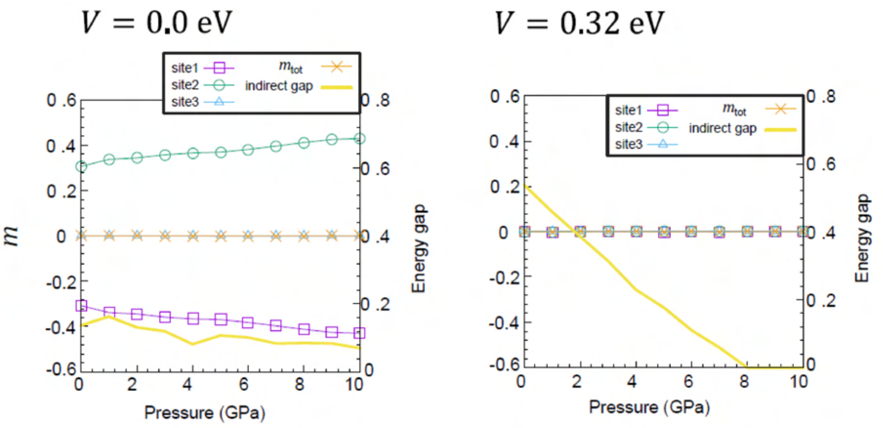

FIG. 5: Pressure dependence of the magnetic moment on each site and the indirect energy gap with the on-site Coulomb interaction $U = 0.7$ eV and with the intersite Coulomb interaction $V = 0$ eV (left) or $V = 0.32$ eV (right).

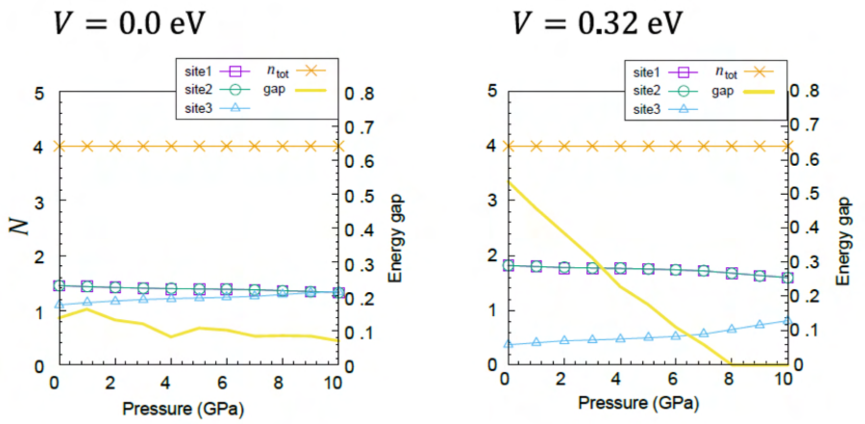

FIG. 6: Pressure dependence of the number of electrons on each site and the indirect energy gap with $U = 0.7$ eV and with $V = 0$=eV (left) or $V = 0.32$ eV (right)

Figures 5 and 6 show the values of magnetic moments and the number of electrons on, respectively, each site and indirect band gap at various pressures with $U = 0$ eV. In case of $V = 0$ eV, the charge distribution among 3 sites is almost uniform (squares, circles or triangles in the left of figure 6). However, the antiparallel magnetic moments appear on site1 and site2 (squares or circles in the left of figure 5) with the finite energy gap (yellow lines in left of figures 5 and 6), which suggests an emergence of an intramolecule antiferromagnetic insulator state as shown in figure 7(a). On the other hand, with $V = 0.32$ eV, the magnetic moments on all sites are zero (crosses in right of figure 5) and both site1 and site2 have the larger number of electrons than site3 (squares, circles or triangles in right of figure 6), which suggests the charge disproportion (figure 7(b)). The energy gap is zero at about 8 GPa pressure, reproducing the crossover pressure observed in the previous study[1].

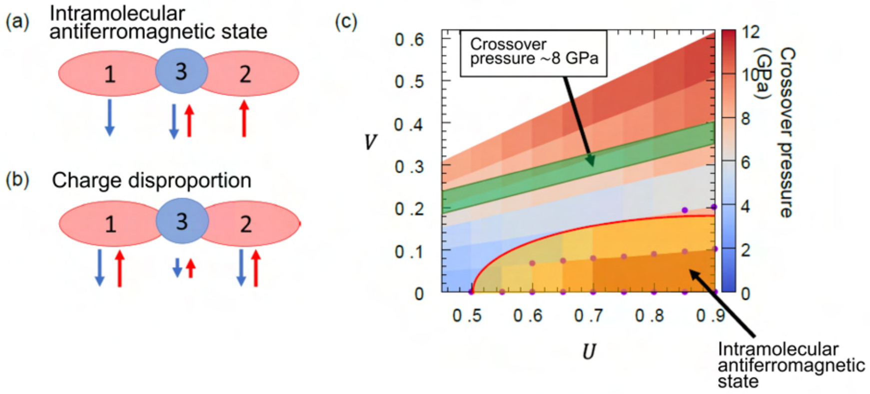

FIG. 7: Intramolecular antiferromagnetic state (a) and a charge disproportion state (b). (c)$U - V$ phase diagram of the crossover pressure. Green and orange signify the regions where the crossover pressure is 8 GPa and where the intramolecular antiferromagnetic state emerges, respectively.

Figure 7(c) exhibits the $U - V$ phase diagram of the crossover pressure. In the green region, the crossover pressure is approximately 8 GPa, where the low-temperature insulator state is a band insulator such as shown in the tight-binding model (figure 4 (a)). On the other hand, in the orange region, intramolecule antiferromagnetic state emerges. V in the orange region is smaller than that in the green region.

The calculations with the extended Hubbard model elucidate that [Ni(hfdt)$_2$] is a non-magnetic band insulator at ambient pressure in the (U, V) region where the crossover pressure of in the previous study is reproduced (the green in figure 7(c)). However, the probability of an intramolecular antiferromagnetic state to emerge is also suggested depending on the values of (U, V). The validity of the calculations is verified by microscopic observation of the electronic state in [Ni(hfdt)$_2$] using the nuclear magnetic resonance (NMR) as described below.

4 ^{19}F-NMR experiment on polycrystalline [Ni(hfdt)$_2$]

4.1 Experiment

^{19}F NMR is used to examine the magnetic structure of [Ni(hfdt)$_2$] in the ambient insulator phase. ^{19}F is $I = 1/2$ spin with a natural abundance of approximately 100 %.

The gyromagneitc ratio is $\gamma_\mathrm{n} = 2\pi \times 40.055$ rad MHz/T. One Ni(hfdt)$_2$ molecule contains four CF$_3$ groups and the two CF$_3$ groups on one hfdt ligand are related with those on the other due to the inversion center on Ni atom (figure 1); thus, there are two crystallographically independent CF$_3$ groups in the crystal.

NMR experiment was performed with the polycrystalline sample of [Ni(hfdt)$_2$] synthesized by Akiko Kobayashi and Biao Zhou in Nihon University (figure 8). The sample is packed in the glass tube using glass wool.

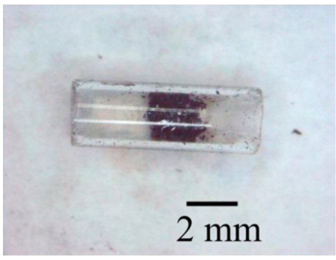

FIG. 8: Picture of a polycrystalline sample of [Ni(hfdt)$_2$]

NMR signals were measured by using the pulse NMR method. The pusle NMR method is a method to shortly observe the NMR signals in the wide frequency range by applying a pulsed AC magnetic field of the Larmor frequency $\sim\gamma_\mathrm{n} H$ within approximately 1 μs time. The shortest AC pulse to induce the NMR is called $\pi/2$ pulse, denoted as $(\pi/2)_x$, where x suggests the x-axis of the rotational coordinate of the Larmor precession. The NMR solid echo signal following the $(\pi/2)_x - (\pi/2)_y$ pulse sequence was Fourier-transformed into NMR spectra. The NMR equipment PROT8111MR (Thamway) was used to apply the AC pulse to the sample and to detect the NMR signals. The nuclear spin-lattice relaxation rate $1/T_1$ was measured by the saturation recover method. Since the relaxation of the nuclear magnetization, $M(t)$, was not single-exponential in time at all temperatures, $1/T_1$ was determined by the single-exponential fitting as follows;

$$1 - M(t)/M(\infty) = A \exp\left[-(t/T_1)^\beta\right] \tag{9}$$

where β is a fitting parameter, indicative the magnitude of the distribution of $1/T_1$ in the polycrystalline sample.

The static external fields of 0.75, 2.5 and 7.5 T were applied by the superconductor magnet. The NMR spectra and $1/T_1$ were measured down to approximately 2 K at ambient pressure.

Because F atoms on the CF$_3$ groups in the Wannier orbitals have closed shells as exhibited in figures 2(a,b), the hyperfine coupling between ^{19}F and conduction electrons is presumed to be vanishingly weak. If the electron spins on the hfdt ligands are strongly polarized such as in the intramolecular antiferromagnetic state suggested in figure 7(a), NMR spectral shifts are expected to be observed because the electron spins yield the semiclassical dipole fileds on the ^{19}F sites (figure 9(a)). In the case of the intramolecule antiferromagnetic state as in figure 7(a), since there are antiparallel magnetic moments on each ligand with the same magnitude, the center of the NMR spectral shift is unchanged and the NMR spectral linewidth is enhanced linearly to the magnitude of the moment (figure 9(b)). In addition, in case of the ferromagnetic state with spontaneous magnetic moments, relatively large NMR specgtral shift should be observed (figure 9(c)). By watching such changes of the NMR spectra, the electronic states on the Ni(hfdt)$_2$ molecules can be understood microscopically.

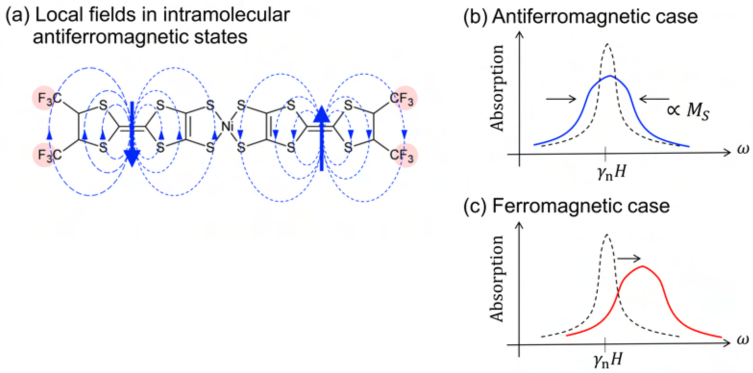

FIG. 9: (a)Electron spins magnetic moments (blue arrows) and local fields yielded by the moments (blue dotted lines) in an intramolecular antiferromagnetic state. (b)^{19}F-NMR spectra in the intramolecular antiferromagnetic moment. Spectra in a para- or a nonmagnetic state are shown by a black dotted line. (c)NMR spectra in a ferromagnetic state

4.2 Results and discussions

Figure 10 shows the NMR spectra under the fields of 0.75 T(a), 2.5 T(b) and 7.5 T(c). The NMR spectral shifts are nearly unchanged on cooling under every field, which suggests that there is no spontaneous magnetic moment as in the ferromagnetic state. Below 120 K temperature under every field, the shapes of the spectra are slightly changed and seem widened on cooling. The temperature dependence of the root of the second moment $\sqrt{\Delta\omega^2}/2\pi$ that characterizes the spectral linewidth is exhibited in figure 11.

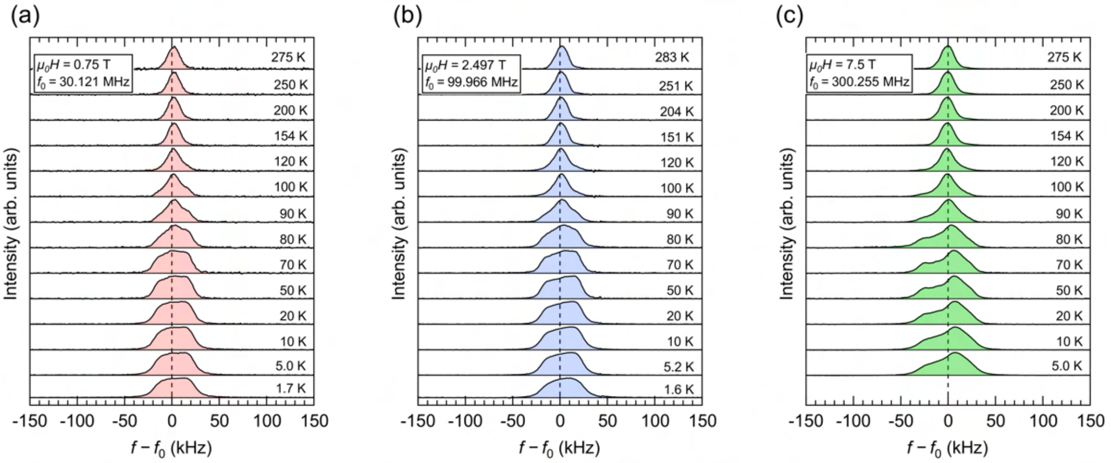

FIG. 10: ^{19}F-NMR spectra of the polycrystalline [Ni(hfdt)$_2$]。Observed frequency were 30.121 MHz under 0.75 T (a), 99.966 MHz under 2.5 T (b) and 300.255 MHz under 7.5 T (c).

The second moments are almost independent of temperature and the magnitude of the field above 120 K. In the temperature range of 80–120 K, the second moments are gradually enhanced, and level off below 80 K at the values of 16–18 kHz.

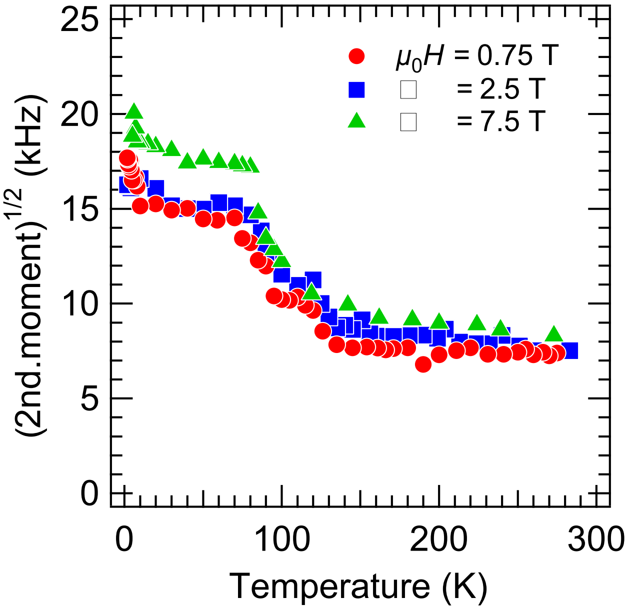

FIG. 11: Temperature dependence of $\sqrt{\Delta\omega^2}/2\pi$ where $\Delta\omega^2$ is the second moment of the NMR spectra.

The values of the second moments are given by a nuclear spin-nuclear spin interaction as

$$\Delta\omega^2 = \frac{\gamma_{\mathrm{n}}^4 \hbar^2}{2} \sum \frac{\left(1 - 3\cos^2\theta_{jk}\right)^2}{r_{jk}^6}, \tag{10}$$

where γ_{n} is the ^{19}F gyromagnetic ratio, $\hbar$ is the reduced Planck constant, r_{jk} is the distance between two ^{19}F spins and θ_{jk} is the angle between the line segment connecting the two ^{19}F spins and the filed direction. For two CF$_3$ groups in a Ni(hfdt)$_2$ molecules, the calculations with the nearest-neighbor nuclear spin interaction using equation (10) yield the spectral linewidths $\sqrt{\Delta\omega^2}/2\pi$ of 15.3 kHz and 17.5 kHz, respectively, which correspond with the experimental values below 80 K. Thus, ^{19}F-NMR spectral linewidth of [Ni(hfdt)$_2$] is dominated by the nuclear spin-nuclear spin interaction but vanishingly contributed by the electron spins, which concludes that there is no intramolecule antiferromagnetic state at ambient pressure. Above 80 K, on the other hand, it is speculated that the nuclear spin-nuclear spin interaction is averaged to be suppressed due to some molecular motions (motional narrowing). Such a molecular motion is a rotational motion of the CF$_3$ group, as discussed with the temperature-dependent $1/T_1$.

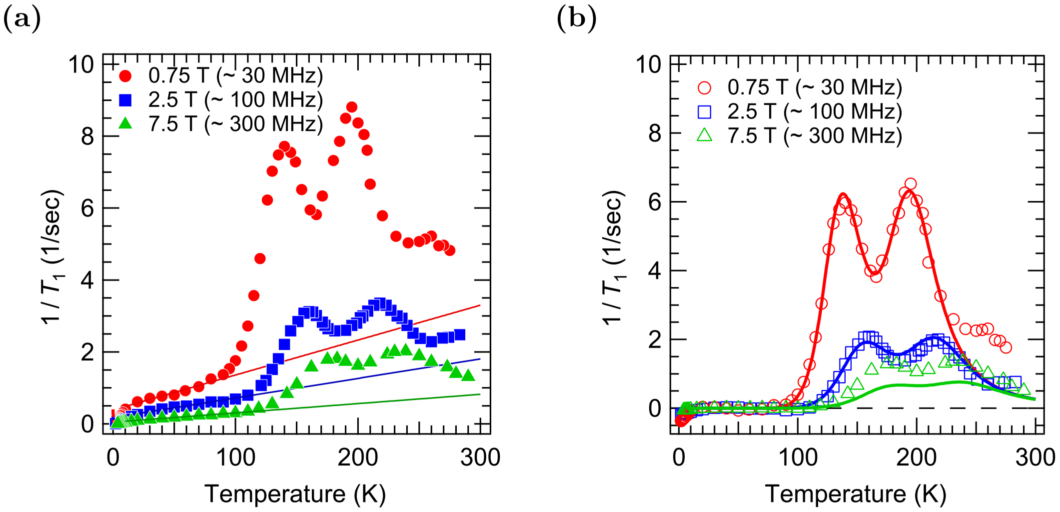

FIG. 12: (a)Temperature dependence of ^{19}F nuclear spin-lattice relaxation rate $1/T_1$. Solid lines signify the result of fitting the values in the range of 20–80 K to a linear function under each field. (b)Result of subtracting the experimental data from the linear functions. Solid lines signify the results of fitting them to the BPP function (see text).

The temperature dependence of $1/T_1$ is displayed in figure 12(a). Two peaks are observed above 80 K under every field. Supposing that the two peaks are contributed by molecular motions, the linear extrapolations using the values of $1/T_1$ in the range of 20–80 K are assumed to be a background of the relaxation (solid lines in figure 12(a)) and subtracted from the experimental values to extract the relaxation component from fluctuations of the molecular motions (figure 12(b)). The subtracted data are fitted to the Bloumbergen-Purcell-Pound (BPP) model function [4]. The BPP model describes

$1/T_1$ in terms of a correlation time of a fluctuation τ and the fitting function with BPP model is determined as follows;

$$\left(\frac{1}{T_1}\right)^{\mathrm{BPP}} = \sum_{i=1,2} C_i \left(\frac{\tau_i}{1+\tau_i^2 \cdot \gamma_{\mathrm{n}}^2 H^2} + \frac{4\tau_i}{1+4\tau_i^2 \cdot \gamma_{\mathrm{n}}^2 H^2} \right). \tag{11}$$

Generally, τ_i decreases on cooling and the function described in equation (11) shows a peak when $\tau_i = \gamma_{\mathrm{n}} H$. τ_i is supposed to be a correlatoin time of a molecular motion fluctuation, whose temperature dependence is assumed as the Arrhenius type,

$$\tau_i(T) = \tau_0^i \exp\left(T_g^i / T\right). \tag{12}$$

τ_i^0 is the correlation time in a high-temperature limit and T_g is the activation temperature. This equation suggests a fluctuation of the nonharmonic molecular motion with a finite energy barrier. The results of the fitting are shown by the solid lines in figure 12(b) and the fitting parameters are in table 1.

$i =$	1 (low-T)	2 (high-T)
C_i (rad$^2\cdot$ kHz^2)	815	738
τ_0^i (ps)	0.18	0.024
T_g^i (K)	1346	2312

TABLE 1: Prameters for the fitting with the BPP model.

A rotational motion of a CF_3 (or methyl) group is known as such a molecular motion represented by the BPP model. ^{19}F nuclear spins on the CF_3 group nonharmonically oscillate among three levels degenerated by a three-fold rotation operation. The oscillation fluctuation should yield the nuclear spins relaxation. The relaxations by the rotational motion of the CF_3 groups were observed in $[(\text{-}C_6H_4NH\text{-})(CF_3)SO_3)_{0.5}\cdot 0.5H_2O]$ (T_g = 1322 K)[5], $[Cu_4(CF_3COO)_4]\cdot 2C_6H_6]$ (T_g = 660 K)[6] and $[(C_4H_3N)(CF_3SO_3)_{0.3}\cdot 0.36\ H_2O]_n$ (T_g = 900 K)[7]. The values of the activation temperature T_g in the previous studies are close to those in the present experiment (table 1), which indicates that the rotational motion of CF_3 group dominates the relaxation in [Ni(hfdt)$_2$] above 80 K. However, in the previous studies, only one kind of the peak of $1/T_1$ was observed. The reason why the two peaks are observed in [Ni(hfdt)$_2$] is that there are two crystallographycally independent CF_3 groups in a molecule (figure 1).

The temperature dependence of the NMR spectral linewidths and of $1/T_1$ can be interpreted as follows; as the nonharmonic rotational motion of the CF_3 groups slow down on cooling from room temperature, $1/T_1$ takes a peak at the temperature where an inverse of the correlation time of the rotational fluctuation $1/\tau_i$ is equal to the Larmor frequency $\gamma_{\mathrm{n}} H$ (figure 12(a)). The rotational motions are averaging the nuclear spin-nuclear spin interaction to suppress its contribution to the spectral linewidths (motional narrowing). After $1/T_1$ takes the low-temperature peak (120–180 K), the correlation time τ_1 increases to a value close to the NMR coherense time T_2. This slowing down of the rotational motion restores the contribution of the nuclear spin-nuclear spin interaction to the spectral linewidths (figure 11). Lastly, the rotational motion of the CF_3 groups is frozen and the NMR spectral linewidths level off the value determine by equation (10). Indeed, the temperature at which $1/\tau_1(T)$ is the same as $\sqrt{\Delta\omega^2}$ ($\sim 1/T_2$) is estimated $T \simeq 70$ K by using the experimental value under the field of 7.5 T and the fitting parameter of $i = 1$ in table 1. This temperature is almost equal to the temperature where the linewidth levels off (figure 11), which strongly supports the above discussion and reasonability of the BPP model.

Although the extrapolation using the values of $1/T_1$ in the range of 20–80 K was subtracted from the experimental data for the BPP model fitting (figure 12(a)), the linear-to-temperature relaxation rate is unclear. Such a relaxation may be produced by fluctuations of impurity spins. When there are some impurity spins in the sample, the thermal fluctuations of the impurity spins, whose energy levels are Zeeman-split under a magnetic field, cause the relaxations of the nearby nuclear spins. $1/T_1$ in the low temperature region is shown in figure 13 by the Arrhenius plot.

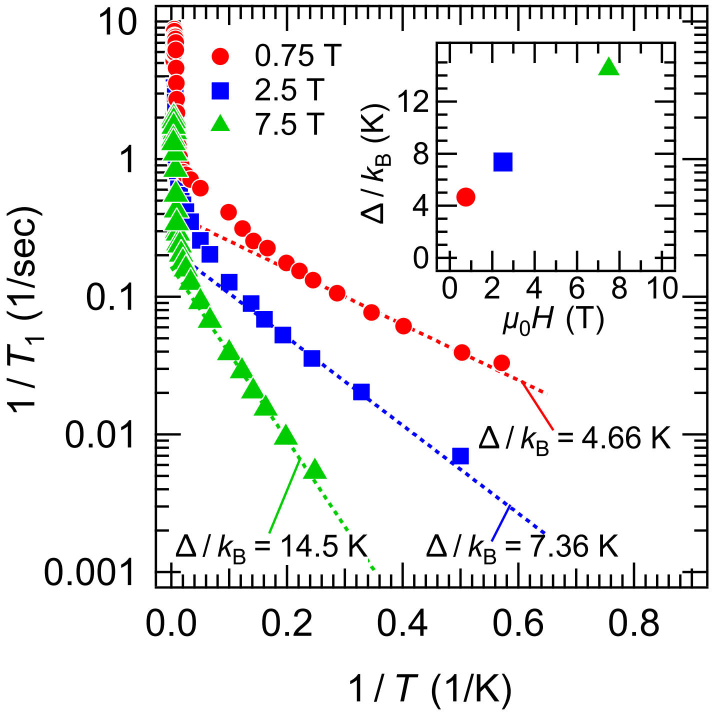

FIG. 13: Arrhenius plot of $1/T_1$. Dotted lines signify the fitting with exponential functions $A\exp(-\Delta/k_BT)$. (Inset)$\mu_0 H$ dependence of activation enegy Δ/k_B

Under an each magnetic filed, $1/T_1$ is exponentially reduced below 10 K. The dotted lines in figure 13 are the results of the fitting by the exponential functions $A\exp(-\Delta/k_BT)$. As discussed above, if the Zeeman-split impurity spins determine the values of $1/T_1$ in the low temperature regions, the activation energy Δ should correspond with the Zeemanspit energy, which is proportional to the magnitude of the magnetic field. However, the activation energy does not appear to be zero in the zero-filed limit as shown in the inset of figure 13, despite its linearity to the field. Thus, we cannot claim that the low-temperature relaxation is caused by the fluctuations of the impurity spins. With considering the linear-to-tempeature $1/T_1$ in the range of 20–80 K, it is needed to study more on the relaxation mechanism in [Ni(hfdt)$_2$] in the temperature range where the CF$_3$ rotational motions are frozen.

5 Conclusion

We study the electronic state of the novel Dirac NL semimetal [Ni(hfdt)$_2$] in the ambient insulator phase both theoretically and experimentally. The analysis of the electronic state with applying the mean-field approximation to the extended Hubbard model elucidates that [Ni(hfdt)$_2$] is a band insulator in the range of (U, V) where the crossover pressure from a metallic state to an insulator state in the previous study is reproduced [1]. In addition, the probability of an intramolecular antiferromagnetic state to emerge is also suggested depending on the values of (U, V). By performing the ^{19}F-NMR experiment, the NMR spectra and $1/T_1$ are measured under the fields of 0.75, 2.5 and 7.5 T. No significant NMR spectral shifts are observed and the spectral linewidths are well interpreted by the nuclear spin-nuclear spin interaction under every field. Thus, it is concluded that there is no magnetic ordered state with strongly polarized electron spins in the low temperature. $1/T_1$ shows two peaks above 80 K temperature, which are reproduced well by the BPP model considering the rotational motion of the CF$_3$ groups. Any enhancement of the spin fluctuation as indication of a magnetic transition are not observed. The experimental result proves [Ni(hfdt)$_2$] to be a nonmagnetic insulator at ambient pressure, which is consistent with the band insulator suggested by the theoretical calculations.

However, as the ^{19}F-NMR experiment does not reveal an origin of the linear-to-temperature $1/T_1$ in the range of 20–80 K, there is much room for investigations of the low-temperature electronic state in [Ni(hfdt)$_2$]. The future work is to explore what electronic states contribute emergence of the Dirac NLs and the superconducting state with pressure.

6 Acknowledgments

We would like to thank Professor Kazushi Kanoda in University of Tokyo and Associate Professor Akito Kobayashi in Nagoya University for their support and direction of the present study, and thank Professor Akiko Kobayashi and Professor Biao Zhou in Nihon University for precious samples of [Ni(hfdt)$_2$] for the NMR study. Lastly, we would appreciate Professor Kyoko Ishizaka and MERIT program for giving the opportunity to conduct this joint study.

References

[1] H. Cui *et al.*, *J. Am. Chem. Soc.*, **136**, 7619 (2014).

[2] R. Kato *et al.*, *J. Am. Chem. Soc.*, **139**, 1770 (2017).

[3] B. Zhou *et al.*, *Chem. Commun.*, **55**, 3327 (2019).

[4] N. Bloembergen *et al.*, *Phys. Rev.* **73**, 679 (1947).

[5] M. Iida *et al.*, *Synth. Met.*, **47**, 202 (1992).

[6] A. Kubo *et al.*, *Bull. Chem. Soc. Jpn.*, **58**, 2947 (1985).

[7] M. Mizuno *et al.*, *Bull. Chem. Soc. Jpn.*, **63**, 3323 (1990).